

# High Fidelity Multidisciplinary Tool Development for Helicopter Quieting

C.-L. Chen<sup>1</sup>, Ya-Chi Chen and Bing Chen  
*Teledyne Scientific, Thousand Oaks, CA, 91360*

Rohit K. Jain  
*HyPerComp, Westlake Village, CA, 91362*

Tom Lund and Hongwu Zhao  
*University of Colorado, Boulder, CO, 80309*

Z.-J. Wang and Yuzhi Sun  
*Iowa State University, Ames, IA, 50011*

Hossein Saberi  
*Advanced Rotorcraft Technology, Mountain View, CA, 94043*

*and*

T.-H. Shih  
*Ohio Aerospace Institute, Brookpark, OH, 44142*

Flows over helicopter blades are very complex and turbulent. The blades experience dramatically different flow fields at various azimuthal angles. Also, a rotor normally consists of many elastic blades, with a strong coupling between aerodynamics and structure. The problem is indeed multidisciplinary. Current helicopter blade designers use computational models, which depend heavily on experimental data and cannot be used to predict any novel design, which is a significant departure from existing designs. To simulate this multiscale and multidisciplinary physics with confidence, we have developed a robust multidisciplinary computational tool called WINDUS-HELI based on the WIND-US code by coupling CFD with CSD, adopting state-of-the-art numerical approaches, and applying high fidelity physics models. Very reasonable results have been obtained for both the aerodynamic loads/performance and acoustics predictions for all the validation cases studied.

## I. Discussion of Software Capability

### A. WIND-US Enhancement

The WIND-US code was chosen for this study due to the fact that it has the capability of solving the Navier-Stokes equations on a computational domain that is discretized using an arbitrary combination of structured and unstructured grids. [Mani et. al.] In addition, the code can handle possible overlapping grids in the interior of the domain, which is very desirable for hybrid URANS/LES simulations and for the development of novel blade shapes. In this work, the enhancements made for WINDUS-HELI code include second-order temporal accuracy and global-Newton-iterations with dual-time-stepping, moving-grid capability for rotation and translation of rotor [Jain et. al.], unstructured-mesh-deformation for controls motion and elastic deformation of the rotor blades, parallel efficiency improvement, multi-grid scheme, anisotropic non-linear  $\kappa$ - $\epsilon$  model [Shih et. al.], DES model, PRNS models [Shih et. al.] and a free wake model. Interfaces have also been developed in WINDUS-HELI for RCAS [Saberi et. al.] and PSU-WOPWOP codes for flow structure interaction and acoustics signature predictions [Figure 1a]. A sleep-awake

---

<sup>1</sup> Manager, Applied Computational Physics, 1049 Camino Dos Rios/A30, and AIAA Associate Fellow.

mechanism was implemented in WINDUS-HELI for loose coupling with RCAS [Figure 1b]. The loose coupling process starts from RCAS that trims the model with internal aerodynamics. After multiple periodic steady state calculations, RCAS outputs the first blade motion file and creates the flag to inform WINDUS-HELI that the motion file is ready and goes to sleep waiting for the airloads flag. The WINDUS-HELI master processor reads the motion file, updates the cubic spline coefficients used for interpolation and broadcasts this information to all the slave processes and starts the CFD calculation. For a 4-bladed rotor, after finishing a quarter revolution, WINDUS-HELI integrates the airloads and outputs the airloads at the specified radial locations, creates the flag to tell RCAS that the airloads file is ready and goes to sleep waiting for the motion flag. When RCAS detects the flag, it wakes up, deletes the flag, reads the updated airloads. RCAS calculates the difference between the CFD airloads and RCAS airloads

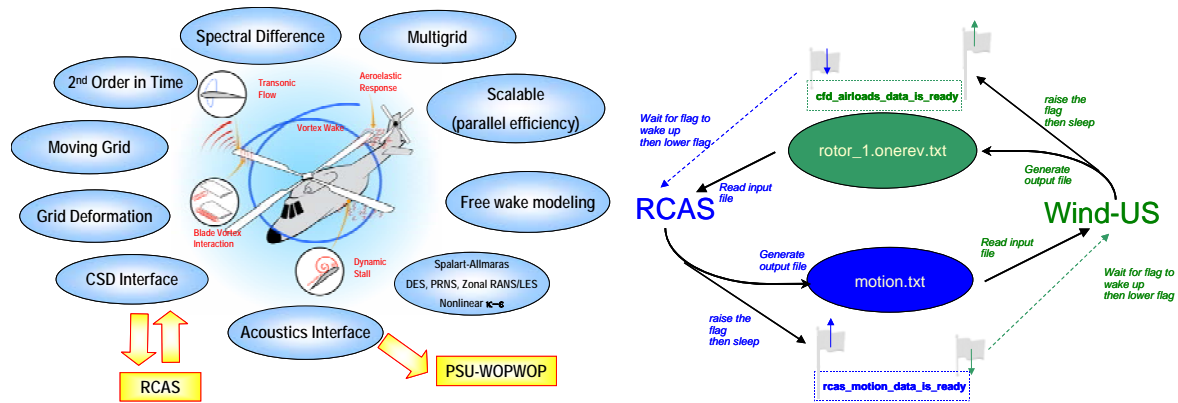


Figure 1. a) WINDUS-HELI code Enhancement, b) automated data exchange mechanism

from the previous trim, and assigns the difference to the mechanical loads. RCAS re-trims with the delta force and outputs the updated motion data and creates the motion flag. WINDUS-HELI detects the flag, wakes up, deletes the flag, reads the motion data and starts the CFD calculation. The whole process is repeated until there is little change in the RCAS and WINDUS-HELI solutions, and convergence is observed in the RCAS trim variables, which consist of collective angle, lateral cyclic angle and longitudinal cyclic angle.

### B. Aeroload Validation

The validation of normal force contour plots of UH-60A cases including C8534, C9017, C9310, C9121, and C9505 are shown in Figures 2-6.

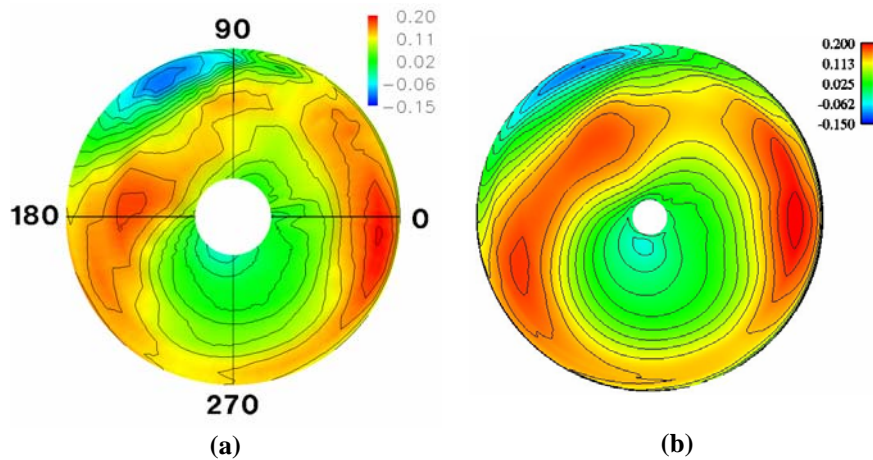


Figure 2. Contour plots of normal force for C8534: (a) Flight test, (b) WINDUS-HELI RCAS coupling.

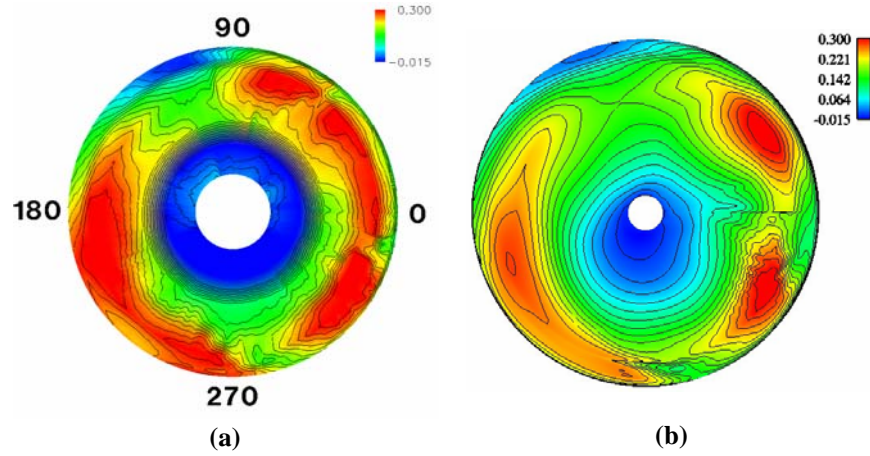


Figure 3. Contour plots of normal force for C9017: (a) Flight test, (b) WINDUS-HELI RCAS coupling.

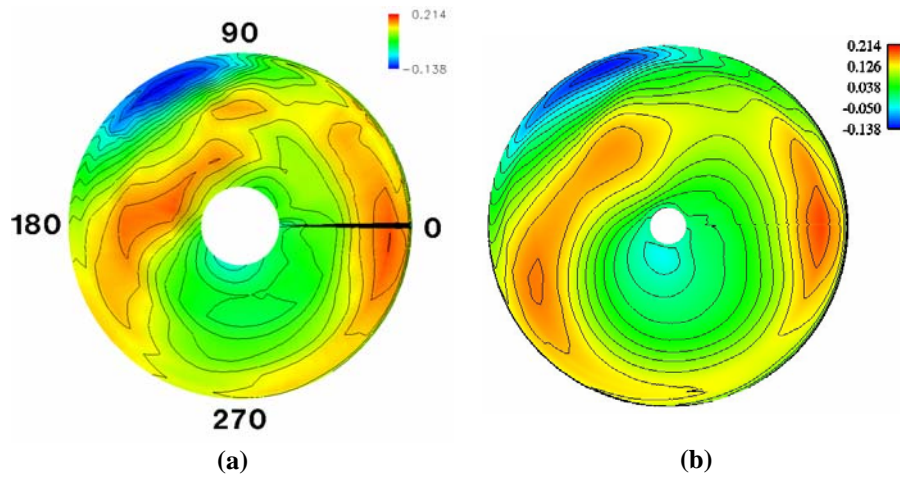


Figure 4. Contour plots of normal force for C9310: (a) Flight test, (b) WINDUS-HELI RCAS coupling.

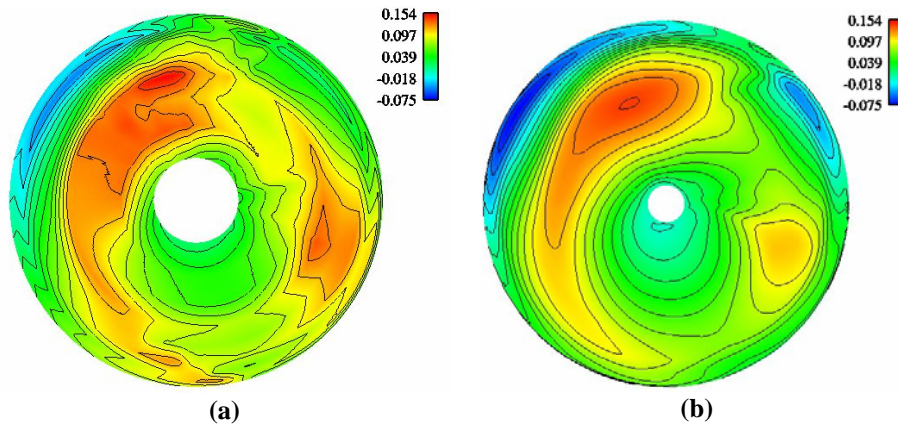
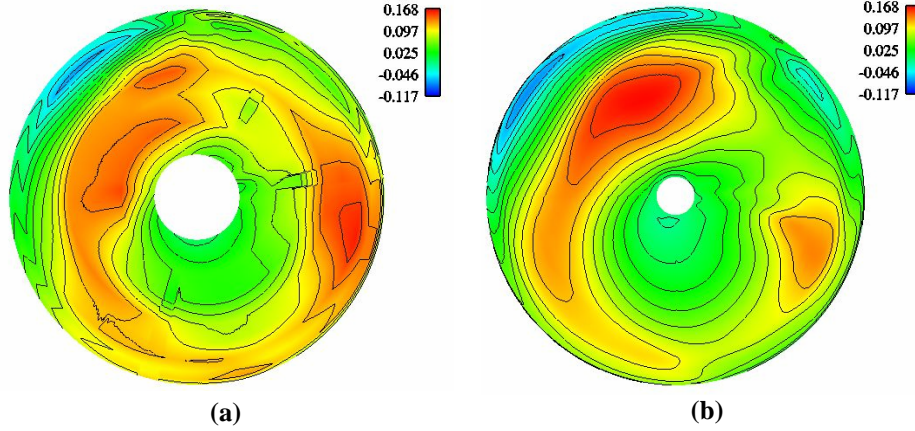
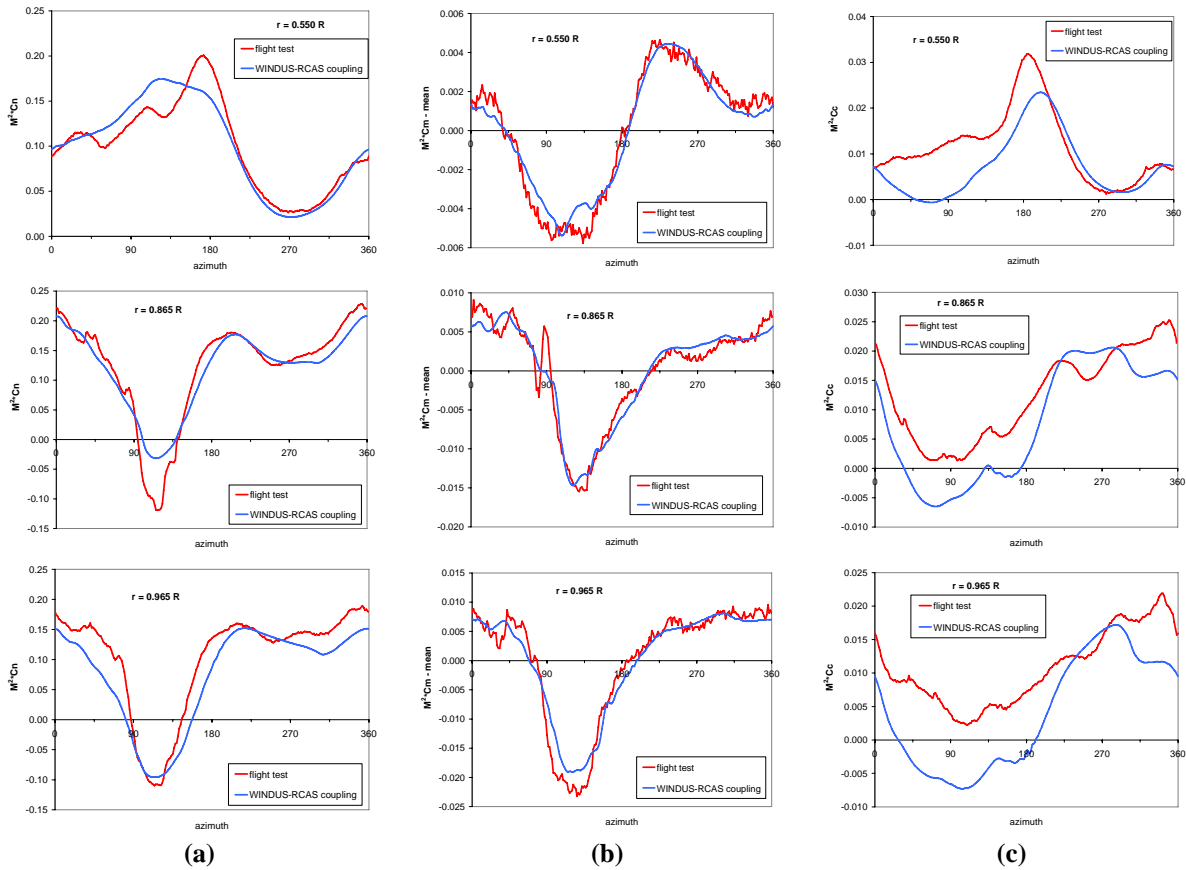


Figure 5. Contour plots of normal force for C9121: (a) Flight test, (b) WINDUS-HELI RCAS coupling.



**Figure 6. Contour plots of normal force for C9505: (a) Flight test, (b) WINDUS-HELI RCAS coupling.**

The airload comparisons for C8534 at three radial locations are shown in Fig. 7. All results are in agreement with flight test data [Kufeld et. al.].



**Figure 7. Airload comparison for C8534 at 55%, 86.5% and 96.5% of radius, (a) normal force, (b) pitching moment, and (c) chord force.**

### C. Acoustics Validation

An acoustics interface has been developed in WINDUS-HELI for performing acoustics signature calculations. The interface has been developed for the acoustics code, PSU-WOPWOP [Hennes et. al.]. Two options are available

for acoustics computations: (a) impermeable surface, and (b) permeable surface. User defines a surface on which flow quantities are interpolated and written out as a sequence of time series. For impermeable surface option, loading (pressure) data are computed on the blade surface as shown in Figure 8. For permeable surface option, flow-field data (density, momentum, and energy) are computed on a surface away from the blade surface as shown in Figure 9.

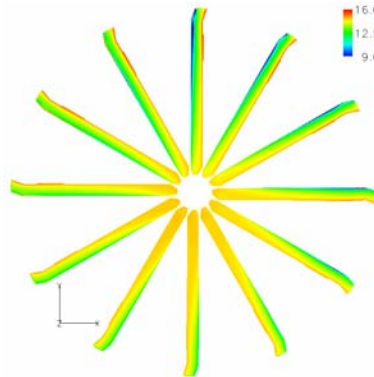


**Figure 8. Impermeable surface approach for acoustics calculations. Time series loading/pressure data are computed on the rotor blade surface.**

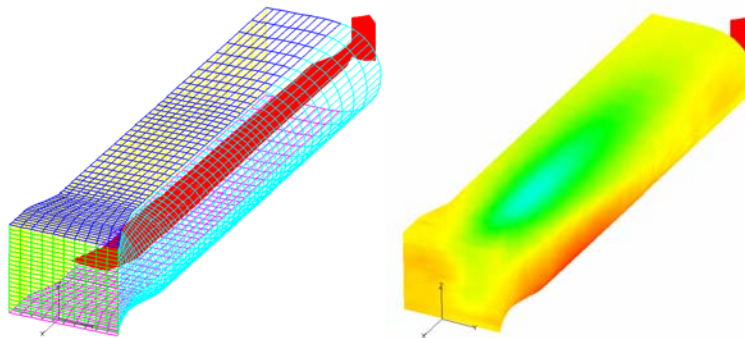


**Figure 9. Permeable surface approach for acoustics calculations. Time series flow-field data is computed on a surface away from the rotor blade.**

It was found that the permeable surface results were very sensitive to the interpolation error and therefore, a special procedure was developed to minimize these errors. For the robustness of the interpolation procedure for the permeable surface option, the relative motion between CFD mesh and acoustics surface should be minimized. Abrupt variations in CFD mesh size (non-smoothed CFD mesh) can lead to large interpolation errors. It was found that such interpolation errors in transferring CFD solution to acoustics surfaces can lead to spurious spikes in the acoustics pressure prediction. Therefore, we have implemented lead-lag, flapping, and pitching motion of the acoustics surface, which causes the permeable surface to follow the CFD mesh very closely, thus minimizing the relative motion between the two. Based on the blade tip motion, collective 1/rev and 2/rev motion are computed and supplied as inputs to WINDUS-HELI. The permeable surface is positioned according to these motion inputs at every time step. The acoustics surface remains rigid (no flexing, only rigid body motions). It was found that the artificial spikes were not encountered if the permeable surface is moved as discussed above.

Acoustics results for the DNW1310 case have been validated. The acoustics calculations were performed at the nine microphone locations using both the permeable and impermeable options and compared with the wind-tunnel measurements supplied by the Government. The permeable surface is shown in Figure 9. The comparison is shown in Figure 10. Both the permeable and impermeable surface results predict the negative peak as well as the phase very well at all the location. The permeable surface option leads to better prediction of the negative peak at microphone location #7. This could be due to the presence of greater high-speed impulsive noise component at this location, which is known to be better captured by the permeable surface option. The positive peak is not well

captured by either option. The reason for this behavior is not understood at this time. The effect of spatial and temporal resolution of the CFD data as well as comparison of the rotating permeable surface (where the surface rotates, flaps, lead-lags, and pitches along with the blade) versus non-rotating surface (where the surface encompasses the entire rotor and does not move with the rotor) needs to be examined to see their effects on predicting the positive peak. Overall very satisfactory agreement with the experimental results was found. The permeable surface generally gives slightly better prediction for this case.

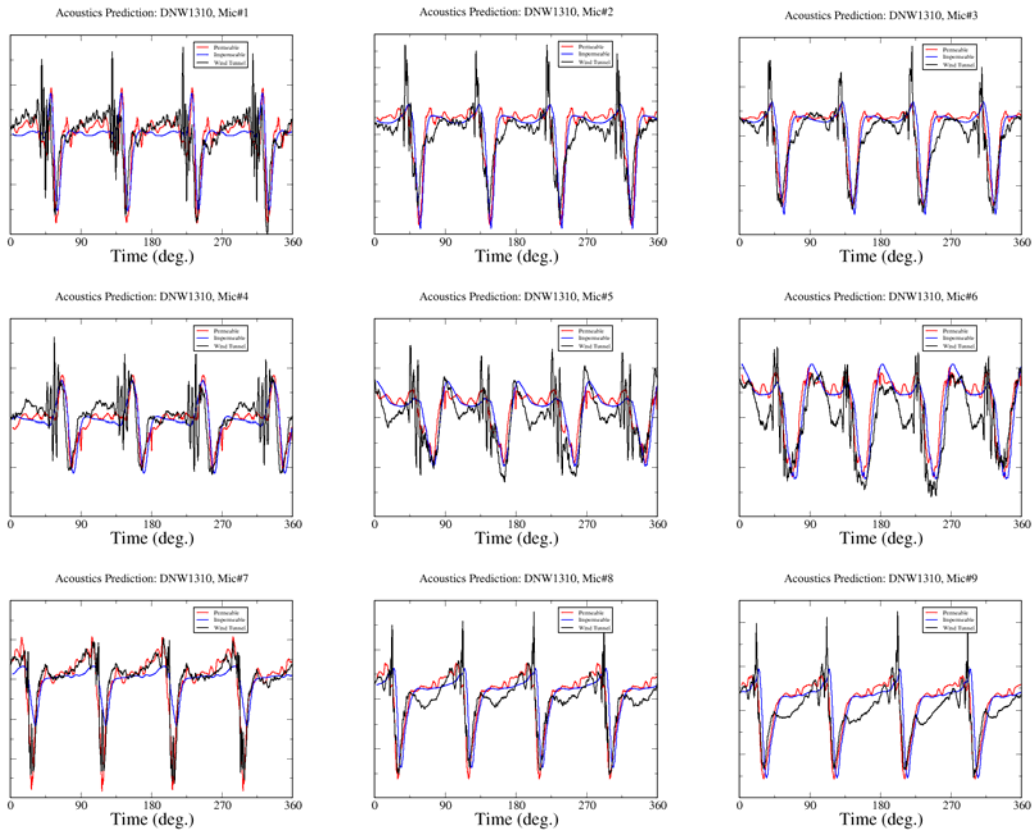


**Figure 10. Permeable surface (red) and impermeable surface (blue) acoustics prediction for case DNW1310 at microphone location 1 thru 9 (in order). Experimental measurement is represented by black curve.**

*1. Acoustics validation of “blind” test cases*

In addition to the DNW1310 cases, acoustics calculations were made for three UH-60A level flight cases listed below

- 1) C9310
- 2) C9121
- 3) C9505

Acoustics data were reported in the form of time history data and frequency data. The time history data (total acoustics pressure) were reported in Pascals for a full rotation at 1024 locations. The frequency data were reported as a single sided power spectrum. The power spectrum is defined as the power spectral density times the frequency bin-width of the Fourier analysis. The data were reported on a hemisphere of radius 100 ft centered at the rotor hub (see Figure 11) every 5 degrees in theta and phi. The theta angle defines the angle under the vehicle and varies from 5 deg (nose) to 175 deg (tail) in 5-degree increments. The phi angle defines the sideline angle. It varies from -90 deg (starboard) to 90 deg (port) in 5-degree increments.

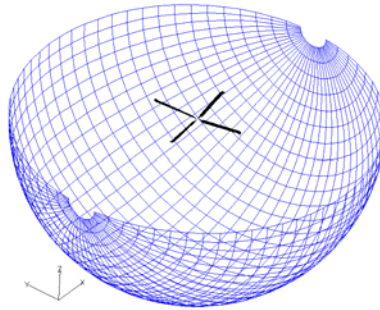


**Figure 11. Hemisphere of radius 100 ft below the rotor centered at the rotor hub for computing acoustics data for the "blind" test cases.**

The data were evaluated against the flight test data. Acoustics prediction for the three cases at a point three rotor radius distance from the hub directly ahead is shown in Figure 12.

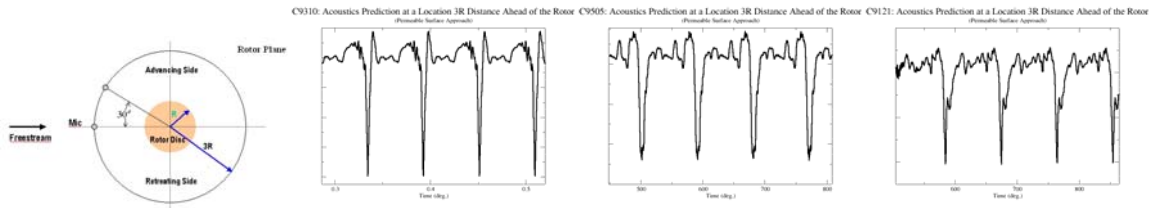


**Figure 12. Acoustics pressure at a test point directly ahead of the rotor in the rotor plane at a distance of three rotor radius. Cases C9310, C9505, and C9121 (from left to right).**

#### D. Turbulence Modeling

The focus of this effort was to introduce state of the art turbulence modeling into the WINDUS-HELI code. When the program began, the only appropriate turbulence model available in WIND-US was the Spalart-Allmaras model. By the end of the program, the code had evolved to a point where the user can chose between various classes of detached eddy simulation models (DES), a non-linear k- $\epsilon$  model (NLKE), and various forms of large eddy simulation models (LES). The various models were validated in a variety of flows including flow over a circular cylinder, flow in a diffuser, static airfoil stall, dynamic airfoil stall, hovering rotor, rotor in forward flight, rotor in forward flight including dynamic stall. The turbulence models available in WINDUS-HELI are as follows:

- 1) Spalart-Allmaras
- 2) Detached eddy simulation (DES)
- 3) Partially-resolved Navier-Stokes (PRNS)
- 4) Detached partially-resolved Navier-Stokes (DETPRNS)
- 5) Non-linear k- $\epsilon$  model (NLKE)
- 6) Smagorinsky subgrid-scale (SGS) model for large eddy simulation (LES)
- 7) Dynamic Smagorinsky (SGS) model for LES (DLES)
- 8) Capability for assigning distinct models to individual zones, most often used with zonal LES (ZLES)

Flow over a circular cylinder was used as an initial validation for the various turbulence models. The topology of the wake is an indication of the range of turbulent motions that can be simulated directly with the hybrid (DES, PRNS) and LES models and the Strouhal number provides a quantitative measure of the model performance. Figure 13 shows a comparison of the cylinder wake flows for the Spalart-Allmaras and DES models. The increased range of resolved scales in the case of the DES model is evident.

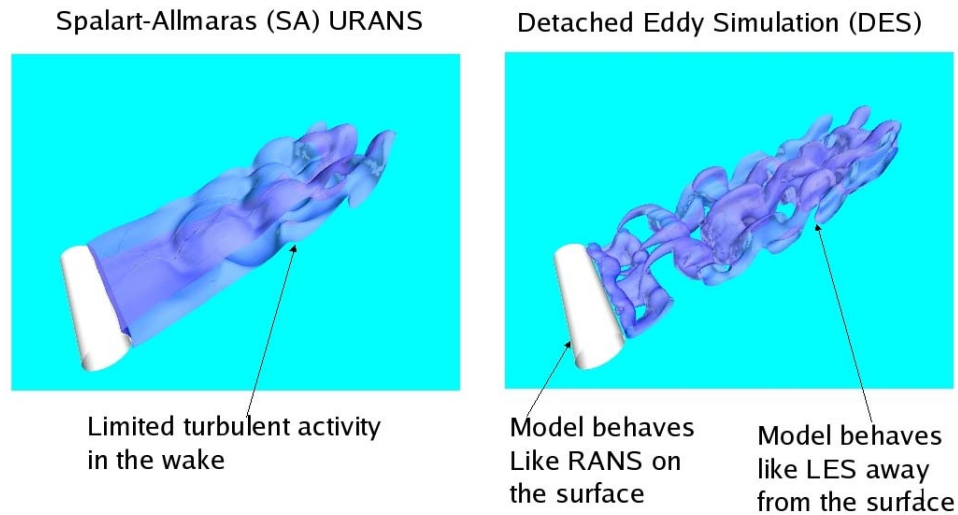


**Figure 13. Comparison of a circular cylinder wake flow using the Spalart-Allmaras and DES models.**

The next validation step was static and dynamic airfoil stall. The experimental data of McCroskey et al. were used as a basis for comparison. Figure 14 shows a set of static stall results for a NACA 0012 airfoil at Mach 0.3. All turbulence models tested were able to reproduce the stall with good accuracy. The dynamic stall cases proved to be much more difficult and accurate results were obtained only after systematic studies of the effects of wind tunnel walls, time step, iteration tolerance, numerical dissipation parameters, and turbulence model. Figure 15 shows a summary of the final results for a deep dynamic stall case with  $\alpha = 15 + 10 \sin(\omega t)$  and reduced frequency  $k = 0.1$ . The Spalart-Allmaras and DES models proved to be reasonably accurate, whereas the PRNS model proved to be less accurate. These results were obtained with a mesh that faithfully represented the wind tunnel walls. The time step was set to  $1/3600^{\text{th}}$  of an oscillation period.

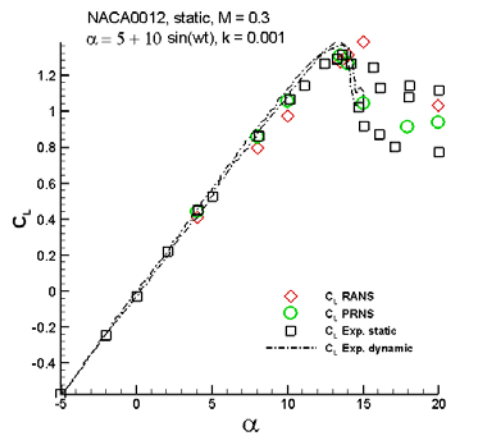


**Figure 14. Static stall of a NACA 0012 airfoil at M=0.3.**

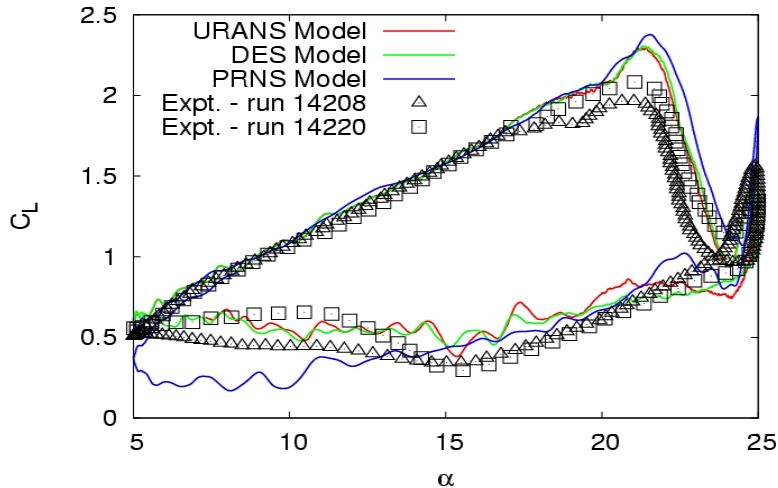


**Figure 15. Dynamic stall of a NACA 0012 airfoil at  $M=0.3$ ,  $\alpha=15+10\sin(\omega t)$  and reduced frequency  $k=0.1$ .**

20 Newton iterations were used with 10 subiterations. The smoothing (numerical dissipation) parameters were set at (0.1,1.0,5.0). The solutions were found to degrade if any of the parameters quoted above were adjusted in a direction that would increase numerical error (such as increasing the time step or increasing the numerical dissipation).

The various turbulence models were also tested in the hovering rotor case of Caradonna and Tung. Figure 16 shows a typical comparison for the blade loading at the 80% radial station. The results were found to depend very little on the turbulence model.

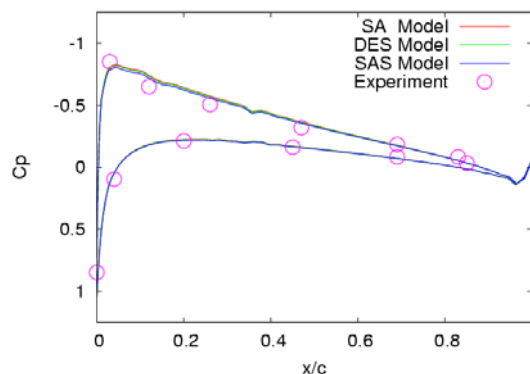


**Figure 16. Pressure distribution on the Caradonna and Tung hovering rotor at the 80% radial station.**

The non-linear  $k-\epsilon$  model was developed late in the program and was not subjected to the validation tests discussed above. It was found to give more accurate results for the UH-60A test cases however. By virtue of the non-linear terms, this model is better able to account for the effects of swirl, which enables a much more accurate capturing of the blade tip vortices. This effect is shown in Figure 17 where the computed pressure distribution near the wing tip is compared with the measurements of Chow, Zilliac, and Bradshaw. This plot shows that either the non-linear  $k-\epsilon$  model or the Spalart-Allmaras model with a rotational correction is required to obtain the correct solution in the vicinity of the vortex. Visualizations of the vortex itself show it to be resolved best when the nonlinear  $k-\epsilon$  model is used. Thus this model was adopted for all of the UH-60A test cases.

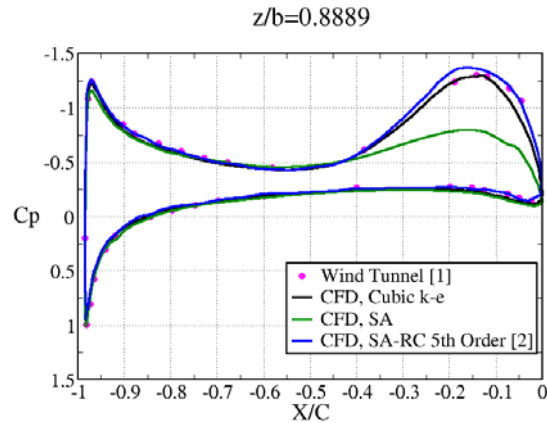


**Figure 17. Pressure distribution very near the tip of the Chow, Zilliac, and Bradshaw wing. The non-linear k- $\epsilon$  model is referred to as the cubic k- $\epsilon$  model in the figure legend.**

### E. Vortex Wake Model

We also implemented a conventional vortex model where the Navier-Stokes computation is limited to within 2-3 chords from the blade surface and the vortex wake model alone is used for the far field. The sketch of the arrangement is shown in Figure 18. The vortex circulation is determined as a function of time from the computed blade loads. The vortex wake is then discretized into a large number of linear segments, which move in time in such a way that the system is always force-free. The velocities induced by the vortex system are fed into the boundary conditions applied on the outer surface of the WINDUS-HELI zone. Figure 19 shows the Navier-Stokes domain for a two-bladed NACA 0012 hover test case. The outer boundary is placed at a distance of two chords away from the blade surface. The computed solutions are compared with the hover measurements of Caradonna and Tung . The blades are set at a collective pitch angle of 8 degrees and the tip Mach number is 0.52.

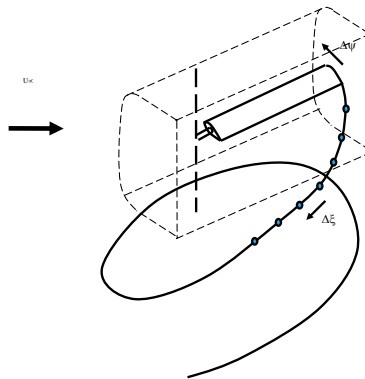


**Figure 18. Schematic of the vortex wake model.**

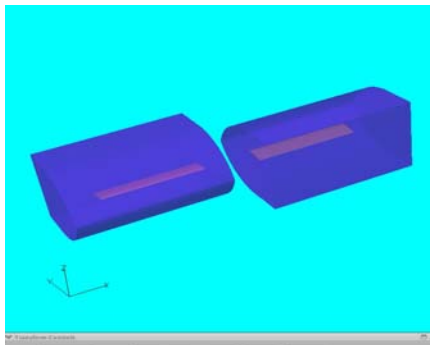


**Figure 19. Navier-Stokes domain for the two-bladed test case.**

Figure 20 shows a comparison of the computed pressure distributions at several different radial stations. Results are shown for a “full domain” case where the vortex wake is computed directly, a case on the small or “partial domain” without a vortex model and finally a case on the partial domain with a vortex model. As expected, the results for the case of the partial domain without a wake model (green curves) show poor agreement with the experimental data. The results are improved greatly for all stations when the wake model is added (blue curve). Finally, the results with the wake model also agree well with the simulation done on the full domain where the wake vortices are computed directly.

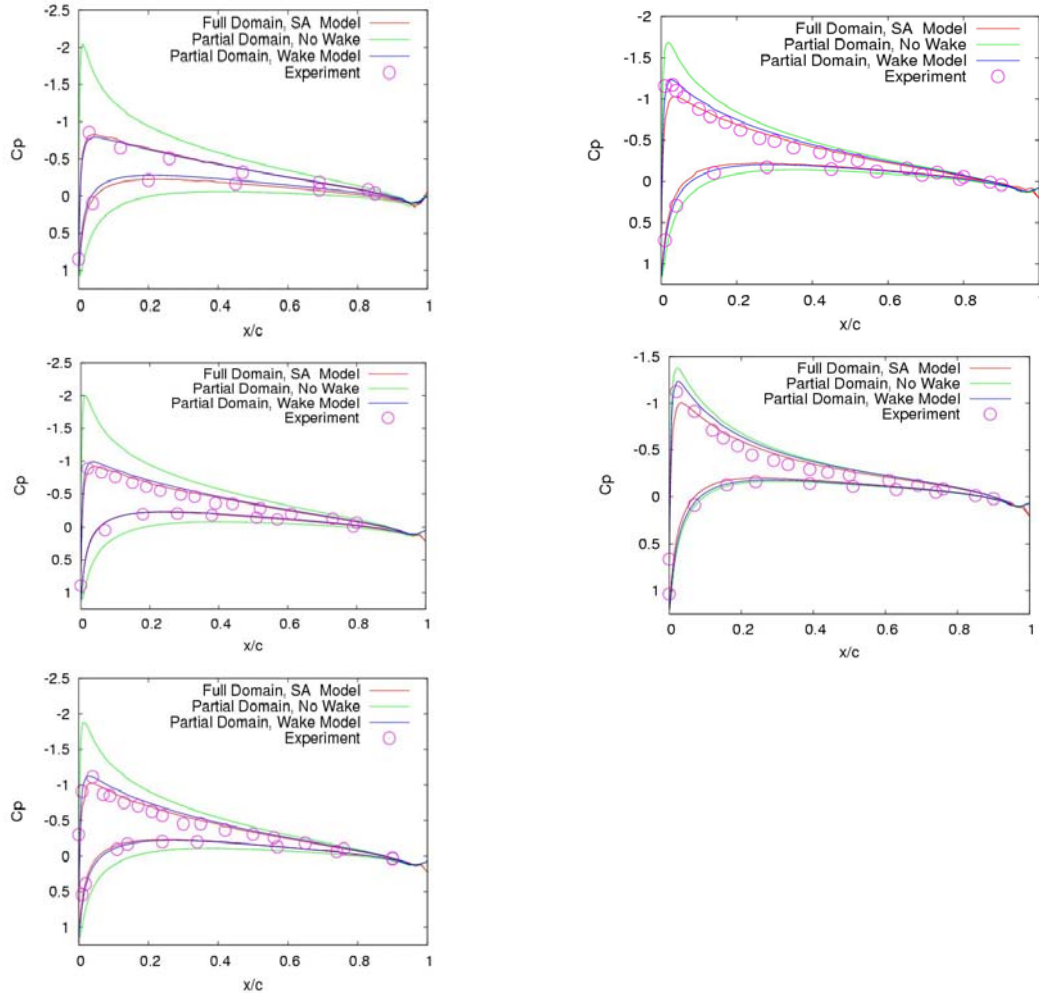


**Figure 20. Comparison of pressure distributions for the NACA 0012 hover case using the vortex wake model. From top to bottom figures and left to right are for  $r/R=0.50, 0.68, 0.80, 0.89,$  and  $0.96$ .**

## F. High-order Spectral Difference Approach

In order to tackle the following challenges in the helicopter flows—interactions between blades, vortex and wakes, complex and dynamic geometries, and disparate length scales—a high order multi-domain spectral difference (SD) method has been developed for the three dimensional Navier-Stokes equations on unstructured hexahedral grids. The code has been verified with the property of high order accuracy and spectral convergence in space; in time integration, the code includes both explicit and implicit schemes. An efficient implicit lower-upper symmetric Gauss-Seidel (LU-SGS) solution algorithm has been developed. The LU-SGS solver is preconditioned by the block element matrix, and the system of equations is then solved with a LU decomposition approach. The implicit solver has shown more than an order of magnitude of speed-up relative to the multi-stage Runge-Kutta time integration scheme for several demonstration problems. The high order curve boundary handling is also included in the code, and the huge difference between low and high order boundary is demonstrated by simulating an inviscid

flow over a sphere. The code has been parallelized and successfully used to run the vortex ring case and the hovering rotor case, which also demonstrates that the code can handle curved boundary with higher order curve surface fitting, possess high resolution of vortices, run the moving grid, and deal with complex geometries. A NACA 0012 two bladed rotor [Caradonna, F.X., and Tung, C.] has been computed with SD code. More than three revolutions of tip vortex trajectories have been observed and the potential of wake capturing has been demonstrated. [Figure 21] The spectral difference code has been integrated into the WINDUS-HELI code, which has been tested on some simple problems.

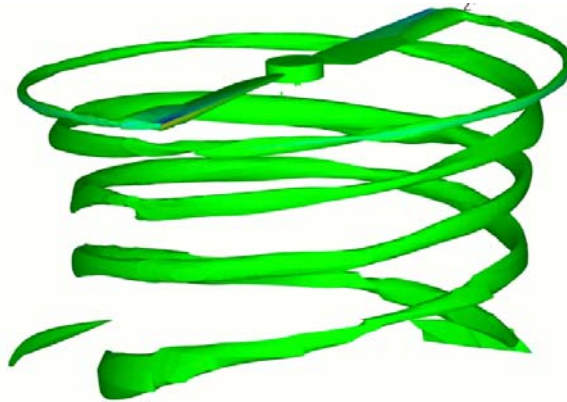


**Figure 21. Iso-surface of down wash**

## **II. Conclusion**

In summary, the WIND-US based helicopter rotor code coupled with RCAS and WOPWOP-PSU has been developed. The UH-60A calculations are in good agreement with experimental data. The high-order spectral difference code demonstrates its potential for capturing the rotor wake. Additional validation of codes for dynamic stall and blade-vortex interaction are still required.

## **Acknowledgements**

This work was sponsored by DARPA under ARO Contract# W911NF-04-C-0102. Opinions, interpretations, conclusions, and recommendations are those of the authors and are not necessarily endorsed by the United States Government. The authors would like to thank the program monitors Dr. Dan Newman, Dr. Steve Walker and Dr. Lisa Porter for their support. The authors would also like to thank Dr. Thomas Doligalski and the HQP review committee for their guidance.

## **References**

- <sup>1</sup> Jain, R.K., Ramakrishnan S.V., and Chen, C.L., "Enhancement of WIND-US for Helicopter Flow Simulation," Presented at the 36<sup>th</sup> Fluid Dynamics Conference and Exhibit, San Francisco, CA, AIAA Paper No. AIAA-2006-3373.
- <sup>2</sup>Shih T.H., Zhu, J., Jiou W., Chen K.H., Liu, N.S., and Lumley J. L., "Modeling of Turbulent Swirling Flows", NASA TM-113112, ICOMP-97-08; CMOTT-97-03, 1997.
- <sup>3</sup>Shih, T.H., Liu, Nan-Suey and Chen, C. L., "A Strategy for Very Large Eddy Simulation of Complex Turbulent Flows," AIAA-2006-0175, 44<sup>th</sup> AIAA Aerospace and Sciences Meeting and Exhibit Conference, Jan. 9-12 2006, Reno Hilton, Reno, Nevada.
- <sup>4</sup>Sun, Y., Wang, Z.J., Liu, Y., and Chen C.L., "Efficient Implicit LU-SGS Scheme for High-Order Spectral Difference Method on Unstructured Hexahedral Grids", AIAA-2007-313.
- <sup>5</sup>Mani, M., Cary, A., and Ramakrishnan, S.V., "A Structured and Hybrid-unstructured Grid Euler and Navier-Stokes Solver for General Geometry," AIAA-2004-524.
- <sup>6</sup>Saberi, H., Khoshlahjeh, M., Ormiston, R. A., and Rutkowski, M. J., "Overview of RCAS and Application to Advanced Rotorcraft Problems," American Helicopter Society 4<sup>th</sup> Decennial Specialist's Conference on Aeromechanics, San Francisco, CA, January 2004.
- <sup>7</sup>Hennes, Chris, WOPWOP User's Guide, The Pennsylvania State University.
- <sup>8</sup>Potsdam M., Yeo H., and Johnson, W., "Rotor Airloads Prediction Using Loose Aerodynamic Coupling", AHS 60<sup>th</sup> Annual Forum.

<sup>9</sup>Liu, S. R. and Marcollni M. A., "The Acoustic Results of a United Technologies Scale Model Helicopter Rotor Tested at DNW", AIAA Paper 90-AHS invited paper at AIAA 13<sup>th</sup> Aeroacoustics Conference, October 1990.

<sup>10</sup>Chen, C.L., McCroskey, W. J., and Ying, S. X., "Euler Solution of Multiblade Rotor Flow," NASA TM-100014 USAAVSCOM TR 87-A-15, 1988.

<sup>11</sup>Caradonna, F.X., and Tung, C., "Experimental and Analytical Studies of a Model Helicopter Rotor in Hover," Vertica, Vol. 5, 1981, 149-161.

<sup>12</sup>Kufeld, R. M., Balough, D. L., Cross, J. L., Studebaker, K. F., Jennison, C. D., and Bousman, W. G., "Flight Testing of the UH60A Airloads Aircraft," American Helicopter Society 50<sup>th</sup> Annual Forum, Washington, D.C., May 1994.

<sup>13</sup>Lorber, P. F., Stauter, R. C., and Landgrebe, A. J., "A Comprehensive Hover Test of the Airloads and Airflow of an Extensively Instrumented Model Helicopter Rotor," American Helicopter 45<sup>th</sup> Annual Forum, Boston, Mass., May 1989.

<sup>14</sup>Chan, W. M., Meakin, R. L., and Potsdam, M. A., "CHSSI Software for Geometrically Complex Unsteady Aerodynamic Applications," AIAA Paper 2001-0593, AIAA 39<sup>th</sup> Aerospace Sciences Meeting and Exhibit, Reno, NV, January 2001.

<sup>15</sup>Lorber, P. F., "Aerodynamic Results of a Pressure-Instrumented Model Rotor Test at the DNW," American Helicopter 46<sup>th</sup> Annual Forum, Washington D.C., May 1990.